



Interlibrary Loan Service

This article is provided by another library and obtained through Interlibrary Loans & Document Delivery Services of the University of Utah's Marriott Library. To use this service, you have agreed to adhere to the University of Utah's Copyright Policy 7-013 (<https://regulations.utah.edu/research/7-013.php>) and the following U.S. Copyright Law restrictions.

IMPORTANT COPYRIGHT INFORMATION

WARNING CONCERNING COPYRIGHT RESTRICTIONS

The copyright law of the United States (Title 17, United States Code) governs the making of photocopies or other reproductions of copyrighted materials. Under certain conditions specified in the law, libraries and archives are authorized to furnish a photocopy or other reproduction. One of these specified conditions is that the photocopy or reproduction is not to be "used for any purpose other than private study, scholarship, or research". If a user makes a request for, or later uses, a photocopy or reproduction for purposes in excess of "fair use", that user may be liable for copyright infringement.

This institution reserves the right to refuse to accept a copying order if, in its judgment, fulfillment of the order would involve violation of copyright law.

*For use as a teaching material, please visit our **Course Reserve** service page <https://lib.utah.edu/services/course-reserves.php> or contact 801-581-6049 or mllib-reserve@lists.utah.edu to receive Fair Use Evaluations and copyright clearance.



Rapid #: -22357988

CROSS REF ID: **1845568**

LENDER: **TEC (Technion) :: Main Library**

BORROWER: **UUM (University of Utah) :: Marriott Library**

TYPE: Book Chapter

BOOK TITLE: 25th AIAA/CEAS Aeroacoustics Conference

USER BOOK TITLE: 25th AIAA/CEAS Aeroacoustics Conference

CHAPTER TITLE: Turbulence Ingestion into a Rotor at the Rear of an Axisymmetric Body

BOOK AUTHOR: Christopher Hickling

EDITION:

VOLUME:

PUBLISHER:

YEAR: 2019

PAGES:

ISBN: 9781624105883

LCCN:

OCLC #:

Processed by RapidX: 4/4/2024 4:07:55 AM

This material may be protected by copyright law (Title 17 U.S. Code)



Turbulence Ingestion into a Rotor at the Rear of an Axisymmetric Body

Christopher Hickling¹, N. Agastya Balantrapu¹, Anthony Millican¹
W. Nathan Alexander², William J. Devenport³
*Center for Research in Experimental Aero/hydrodynamic Technology (CREATe)
Virginia Tech, Blacksburg, VA 24061*

Stewart A.L. Glegg⁴
Florida Atlantic University, Boca Raton, FL 33431

This paper presents the aerodynamic and acoustic measurements of a rotor operating at the rear of an axisymmetric body. The mean flow, turbulence structure and the correlation structure of the undisturbed, axisymmetric, radially inhomogeneous and anisotropic boundary layer has been documented with single hotwire anemometry, Particle Image Velocimetry, and mean and unsteady surface pressure instrumentation. The acoustic farfield of the rotor ingesting this boundary layer has been measured with a 251-channel microphone array, at zero and moderately thrusting advance ratios. For the measured advance ratios, rotor noise was separated from the background using delay and sum beamforming and integrated spectra revealed a broadband noise increase at frequencies above the blade passage frequency (BPF) and the formation of “haystacks” near the BPF and its first two harmonics. The frequencies of the observed “haystack” peaks were shifted higher by ~7-12% of the BPF.

I. Introduction

In many applications, propulsion rotors are required to operate with non-uniform turbulent inflows. The turbulence and non-uniformity excite unsteady loading on the rotor blades and are therefore an efficient source of rotor noise. Examples of this are found in unconventional propulsion arrangements for aircraft as well as in marine propellers and axial pump systems. A particularly illustrative example is in the pusher propeller systems of some light aircraft, such as the Piaggio Aero P180. This has been the subject of extended study under the European Cost-Effective Small Aircraft program (CESAR). This airplane is well known for efficiency and, since the propellers are mounted downstream of the wing, low levels of cabin noise [1]. At the same time exterior noise levels are particularly high because the propellers ingest the wing and flap wakes, the engine exhaust and a relatively thick nacelle boundary layer. These noise-generating flow features are complicated by the upstream influence of the propeller inflow on their formation.

Sevik [2] was amongst the first to tackle the problem of turbulence ingestion noise under steady conditions by considering the simplest case of homogeneous turbulence. He measured the unsteady thrust on a 10-bladed propeller mounted downstream of turbulence generating grids in the Garfield-Thomas Water Tunnel at Penn State. Sevik’s work is important because he was the first to observe ‘haystacking’ – the organization of the broadband spectrum into peaks

¹ Graduate Research Assistant, Kevin T. Crofton Department of Aerospace and Ocean Engineering, AIAA Student Member.

² Assistant Professor, Center for Research in Experimental Aero/hydrodynamic Technology, Kevin T. Crofton Department of Aerospace and Ocean Engineering, AIAA Member.

³ Professor, Center for Research in Experimental Aero/hydrodynamic Technology, Kevin T. Crofton Department of Aerospace and Ocean Engineering, Associate Fellow AIAA.

⁴ Professor, Department of Ocean and Mechanical Engineering, Associate Fellow AIAA.

(or ‘haystacks’) centered on multiples of the blade passing frequency. Haystacks are generated when turbulent structures are cut multiple times by successive blades. Haystacking is enhanced when the ingested turbulence is large compared to the blade spacing or the turbulence is elongated as it is drawn into the rotor [3, 4]. A number of prediction methods incorporating the correlation effects of large scale turbulence have been developed [5-9]. Most of this work has considered homogeneous turbulence, but some considered rotor interaction with an axisymmetric casing boundary layer ingested into the tip region of a shrouded rotor.

The goal of the presented work is to study the sound from a rotor ingesting an inhomogeneous axially symmetric boundary layer developed around the circumference of an upstream body. These data are being compiled in order to produce a validation dataset for aeroacoustic prediction methods of broadband rotor noise particularly for cases where the generation of the upstream turbulence is coupled to the operation of the rotor. To accomplish this, we have designed and fabricated a body of revolution which produces a thick boundary layer on an aft ramp section that is on the verge of separation without aerodynamic influence of the downstream rotor. The evolution and character of the inflow to the rotor has been well documented through hotwire, PIV, and steady as well as unsteady surface pressure measurements. The rotor is positioned at the downstream end of the body in-line with the body’s axis of symmetry and is completely immersed in the body wake at the zero-thrust condition. Flow and acoustic measurements were conducted in order to understand the rotor’s influence and interaction with the thick body boundary layer.

II. Apparatus and Instrumentation

A. Virginia Tech Stability Wind Tunnel

All measurements were made in the Virginia Tech Stability Tunnel, shown in Fig. 1. This closed-circuit facility has a test section 1.83 m square 7.32 m long, and can be operated in two configurations: a conventional hard-wall aerodynamic section and a Kevlar-walled anechoic section. In this study, the wind tunnel is used in its anechoic configuration, described by Devenport et al. [10]. The circuit of the tunnel is anechoically treated in order to minimize the propagation of noise from the fan to the test section. The floor and ceiling of the test section are constructed of tensioned Kevlar cloth structurally supported by perforated metal panels. These panels are backed by foam acoustic absorbers. The walls of the anechoic test section are made of Kevlar tensioned in two large rectangular frames. In this way, the Kevlar is designed to contain the flow while allowing acoustic perturbations to transmit from the test section. Anechoic chambers, 6 m × 2.8 m × 4.2 m, seal against the sides of the test section on both the port and starboard sides and are anechoic down to 190 Hz. Microphone instrumentation can be placed in these chambers to measure the noise produced by models in the test section. The maximum attainable freestream velocity in the test section is 80 m/s. During our experiments the freestream speed varied between 20 – 23 m/s, ensuring a consistent Reynolds number of 600,000 based on the maximum body diameter. The Stability Tunnel has extremely low freestream turbulence levels, $u'/U_\infty \approx 0.02\%$ at 20 m/s. Therefore, the measured aerodynamically generated broadband noise is expected to be dominated by turbulence ingestion from the rotor/boundary layer interaction

B. Body of Revolution (BOR) and Coordinate System

The body of revolution, inspired by the work of Hammache [11], is shown in Fig. 2. The body has a 2:1 elliptical nose which extends forward from a cylindrical section with a diameter of $D = 432$ mm. The cylindrical midsection of the body has a length of one maximum body diameter D and leads to a sharp corner at the beginning of a 20° tail cone. The tail cross section reduces with axial distance down to a section 63.5 mm in diameter at an axial location $1.17D$ downstream of the sharp corner. The rotor is positioned at this station to ingest the thick turbulent boundary layer generated on the body. A circumferential trip ring having a square cross section 0.81 mm x 0.81 mm is positioned close to the downstream end of the elliptical nose in order to induce transition.

Figure 2 also defines the Cartesian coordinate system (x, y, z) to be used throughout the paper. The coordinate system origin is at the nose of the body, and the position x is measured downstream from the nose apex, y is measured from the body centerline vertically upward toward the test section ceiling, and z is measured from the body centerline horizontally to port, completing a right-handed coordinate system. The mean velocities along the x, y, z axes are identified by U, V, W , respectively, and the fluctuating velocities in the lower case variables, u, v, w , respectively. The streamwise mean and fluctuating velocity are denoted by U_s and u_s , respectively. Furthermore, given the axisymmetric character of the body and flow, a cylindrical coordinate system (x, r, θ) has been defined, with r representing the radial distance from the x axis (body of revolution axis) and θ measured according to the right-hand rule.

When installed in the Virginia Tech Stability Wind Tunnel, the body of revolution is suspended from thin steel tethers passing through the body just past the end of the nose. These tethers are mounted in the $x - z$ plane 1.03D downstream from the body nose at approximately 45° from the vertical y axis. Two different sets of tethers were used

during the course of the experiments. Initially, 1.6 mm diameter tethers with symmetric airfoil fairings (6.4 mm chord, 3.2 mm thick) were used, but measurements in the body wake showed that these tethers produced significant wakes at the location of the rotor, $x/D = 3.17$. As such, subsequent testing used smaller but stronger 0.9 mm diameter tethers without fairings. The wake deficit of these new tethers at the rotor location were of approximately half the width of the original design. Detailed measurements of the wake profiles for both tether arrangements are presented in the results (Section IV. A).

In addition to tethers, the body of revolution is supported downstream on a rotor drive sting at the end of the tail section. Two different downstream sting arrangements are used for measurements with and without the rotor (Fig. 3). For measurements without the rotor, a simple static sting support was used to support the model as shown in Fig. 3 (A). For measurements with a rotor, a drive rig replaces this sting which contains a Kollmorgen AKM54L-ACCNDA00 servomotor which drives a hollow shaft with a timing belt Fig. 3 (B). All cables for instrumentation in the body of revolution pass through the center of the drive shaft exiting far downstream of the rotor such that the inflow to the rotor is axially symmetric except for the wakes generated by the supporting tethers. In both configurations, the body is located in nearly the same position within the test section, and the sting support (static or rotating) extends at least 0.76 m downstream of the rotor before reaching the downstream support. Ideal flow and RANS calculations indicate this sting length positions the rotor well outside of the region of significant upstream influence by the downstream support/drive rig.

C. Rotor

The rotor used in this study is custom designed to operate in the BOR boundary layer (Fig. 4). It is a 5-bladed rotor with an outer diameter of 216 mm (equal to $D/2$) and hub diameter of 63.5 mm. The hub diameter was sized to allow instrumentation cabling to pass through the rotor shaft to the BOR, and the rear diameter of the BOR was then matched to that of the rotor hub. The outer diameter of the rotor was chosen to match the boundary layer thickness at the ramp exit plane ($x/D = 3.17$) when $Re_D = 600,000$. The boundary layer thickness at the ramp exit plane was initially predicted with RANS and experimentally confirmed with a $1/4$ scale experiment before full scale manufacture. The zero thrust advance ratio of the rotor is 1.44. The rotor blade pitch is wake adapted to account for the mean velocity distribution in the radial direction at the zero-thrust condition. The rotor has zero total rake, but a maximum sectional skew angle of 35.5° near the tip. At 75% radius, the blades have a maximum thickness of 6 mm, blade pitch of 168 mm, and chord of 57 mm. The rotor was CNC-machined from 6061 Aluminum. The blade sections have a 0.18 mm radius at the trailing edge to aid in manufacturing and a variable radius fillet at the hub junction to reduce stress concentration.

D. Body Pressure Instrumentation

85 half-millimeter diameter pressure taps were embedded into the body of revolution (Fig. 5): 51 ports measured the streamwise mean surface pressure distribution, and 36 ports measured the circumferential uniformity on the nose at $x/D = 0.095$ and 0.5. The pressure was sampled at 100 Hz via Tygon tubes by DTC Initium ESP-32HD acquisition system with a 10" water range and $\pm 0.05\%$ FS accuracy. The body was installed at zero angle of attack within 0.25° by iteratively adjusting the nose position with the tether system, until the pressure measured by the circumferential arrays were uniform.

A linear streamwise-aligned array of 20 Sennheiser electret microphones (type KE-4-211-2) with 1-mm pinholes were flush mounted along the tail cone of the BOR with a nominal spacing of 12.7 mm. These microphones measure the unsteady surface pressure fluctuations on the tail cone of the body and the evolution of the convective surface pressure fluctuations toward the rotor disk plane. They have a flat frequency response up to 20 kHz. A small number of microphones were found to be defective so data at some locations are only available at multiples of this spacing along the body. In all, there were 20 working microphones extending from axial locations on the body from $x/D = 2.41$ to 3.08. Unsteady surface pressure data were recorded with a Bruel & Kjaer LAN-XI data acquisition system sampling at 65536 Hz for 32 seconds.

E. Total Pressure Rake

A custom-built pitot probe rake was used to measure the wake profile downstream of the body at the rotor plane when the rotor was not installed (Fig. 7). The rake consisted of a radial line of 119, 0.5 mm diameter pitot probes positioned across the wake diameter from $r/D = 0.12$ to 0.3 on either side of the sting support. Installed just downstream of the tail cone ($x/D = 3.17$), the rake was rotated 180° about the x axis to 36 angular stations resolving the body of revolution wake profile, including the tether wakes. An Esterline 9816/98RK-1 NetScanner system with a 10" water range and $\pm 0.03\%$ water accuracy, sampled the total pressure, via Tygon tubing.

F. Constant Temperature Hotwire Anemometry

The evolution of the undisturbed axisymmetric turbulent inflow over the body of revolution at $Re_D = 600,000$ was documented using single and four sensor hotwire probes. A single hotwire probe (manufactured by Auspex system) was traversed through the boundary layer, 10 mm upstream of the corner at $x/D = 1.98$, obtaining a 30-point profile, of the streamwise mean velocity, turbulence intensity and unsteady velocity spectra – defining the inflow boundary condition to the tail cone flow. The turbulent flow over the ramp was documented with a dual single-wire probe arrangement, obtaining a 205-point cross section in the $x - z$ plane, covering 15 streamwise stations, beginning 25.4 mm downstream of the corner to the exit of the tail cone (from $x/D = 2.05$ to 3.17). The separation between the two identical probes, was fixed at 18.5 mm along a line inclined by 9.3° from the free stream direction towards the body of revolution axis. While the upstream probe provides the single point statistics, the dual probe arrangement could be used to estimate the convection velocity over the tail cone. Measurements with a four-sensor quadwire probe over the same measurement grid were then used to obtain the 3-component single point velocity statistics, including the 6-component Reynolds stress tensor and unsteady velocity spectra, in addition to the mean velocities. The complete construction, calibration procedures and validation of these AVOP-4-100 probes, manufactured by Auspex Corporation, are discussed by Wittmer et al. [12]. These results are described in more detail by Balantrapu et al. [13].

In addition to the single point measurements, the correlation structure of this axisymmetric, radially inhomogeneous and anisotropic boundary layer was measured just upstream of the rotor ($x/D = 3.17$). Measurements were made with a pair of single hotwires, identical to the ones described earlier, in the conventional anchored probe and traversing probe arrangement. Four anchor points were studied at 40, 65, 75, 85% of the boundary layer thickness and correlations and coherence and phase spectra were measured with the traversing probe separated from these locations along radial and circumferential profiles. The resulting correlations, as a function of frequency and separation, could be used to estimate the radial, circumferential and streamwise length scales of the streamwise velocity.

All measurements were made with the Dantec Streamline 90N10 Constant Temperature Anemometer, using a National Instruments acquisition device (NI DAQ 9225-9191) sampling at 50000 Hz, obtaining 50 independent ensembles, with each ensemble containing 8192 samples. During the hotwire measurements, the probes were calibrated often to account for temperature drift, and the data were corrected during post processing, adopting Bearman's [14] procedure.

G. Particle Image Velocimetry (PIV)

Planar PIV was used to measure the instantaneous flow field in the aft region of the body of revolution, complementing the single and two-point statistics from the hotwire measurements. A Quantel Evergreen double-pulsed 532 nm Nd-YAG laser pulsing at 15 Hz was used to illuminate the x - z plane at $y = 0$ along the tail cone. The region of the body struck by the laser was painted with a Kiton Red 620 dye in order to reduce flare from the surface at the laser wavelength. The flow was seeded with atomized DEHS oil by a LaVision Aerosol Generator to generate particles with a mean diameter of approximately $1 \mu\text{m}$. A LaVision Imager sCMOS camera was positioned in the test section ceiling outside of the flow behind acrylic windows and focused on the measurement plane. The camera was manually moved on a linear slide in a plane parallel to the $x - z$ plane to cover multiple fields of interest along the back third of the body tail cone. 6000 image pairs were acquired for each field of interest.

H. 251-Channel Microphone Array

A 251-channel microphone array was positioned in the starboard anechoic chamber of the Virginia Tech Stability Wind Tunnel as shown in Fig. 8. This array employs GRAS type 40PH-S5 $\frac{1}{4}$ " microphones with a dynamic range of 32 to 135 dB(A) and sensitivity of 50 mV/Pa. The microphones in the array are arranged in four interlocking logarithmic spiral patterns centered about different streamwise locations along the length of the test section. The outer limits of the array are contained within a rectangular area of 3.66 m x 1.75 m. The microphone pattern has a minimum separation distance of 29.8 mm and maximum distance of 3.82 m between sensors. Microphone data were acquired at 51200 Hz for a duration of 32 seconds at each condition using a custom data acquisition system.

I. Test Matrix with Rotor

After documenting the detailed undisturbed inflow (without the rotor), the far-field noise of the rotor ingesting the inflow was measured at a detailed set of 65 operating conditions, including 26 advance ratios. In this paper, we present the initial measurements for a fixed Re_D of 600,000 where the rotor speed was varied to obtain the advance ratios shown below, including braking, zero thrust and thrusting conditions. The rotor phase was measured with an auxiliary channel of the array acquisition system, although, the data acquisition was not synchronized with the rotor rotation

rate. Additionally, the measured mean pressure distribution over the body and unsteady pressure distribution over the tail cone were measured to document the inflow distortion by the rotor as a function of the advance ratio.

Table 1. Test matrix for variation with advance ratio at $Re_D = 600,000$

Rotor Speed (RPM)	2136	2725	3299	3687	3926	4020	4113	4220	4314	4442	4535	4701	4782	4992	5128
Advance Ratio J	2.64	2.07	1.71	1.53	1.44	1.40	1.37	1.34	1.31	1.27	1.24	1.20	1.18	1.13	1.10

III. Analysis, Results and Discussion

A. Body of Revolution Flow with Rotor Absent

Fig. 9 shows the streamwise variation of the mean pressure coefficient over the body. The measured distribution compares well with results from RANS calculations [15] and potential flow simulations performed over the BOR at a zero angle of attack, using an inviscid, 3-dimensional doublet panel method. The flow accelerates over the nose, passing the trip ring sandwiched between the nose and the constant diameter mid-body. Further downstream, the sharp corner between the midbody and the tail cone generates an intense local acceleration as the flow enters the tail cone region. Hereafter, the flow decelerates rapidly over the 20° tail cone with the turbulent boundary layer resisting a strong adverse pressure gradient.

The flow over the tail cone exit ($x/D = 3.17$) at the rotor inflow plane, appears axially symmetric excluding the tether wakes, revealed by the stagnation pressure cross-section, shown in Fig. 10 a). Outside the BOR boundary layer, the tether wakes were 23 mm (0.05 D) wide at the tail cone exit. However, subsequent measurements used improved tethers, high strength 0.9 mm steel cables (Section II.B), resulting in much milder wakes, half the size of initial tether wakes. Single hotwire measurements over a quadrant at the tail cone exit plane, using the new tethers, are shown in Fig. 10 b). The streamwise mean velocity in the boundary layer is axisymmetric to 2% and the corresponding turbulence intensity, not included here, is axisymmetric to 7%. Furthermore, outside the BOR boundary layer, the new tether wake suffered a 5% velocity deficit with peak turbulent intensity quite low at 1.5%. These new tethers were employed during the acoustic measurements with the rotor installed.

Since the flow is axially symmetric, we can study the evolution of the turbulent structure by examining a streamwise cross-section through the boundary layer, at a single circumferential location (sufficiently far from the tether regions). All measurements discussed below were made in the horizontal plane ($x - z$) through the nose of the body, unless noted otherwise. First, we shall examine the boundary layer just before it enters the adverse pressure gradient region, 10 mm upstream of the intersection between the mid-body and tail cone, referred to as the corner. The structure of the streamwise mean velocity (U_s) is illustrated in Fig. 11 a) with the vertical axis representing the height from the local surface, normalized by the BOR diameter. The boundary layer thickness (δ) is about 7.9 mm estimated as the height from the surface to where the streamwise turbulence intensity is about 2%. The peak measured streamwise normal stress reaches a value of $0.006 U_\infty^2$, around 0.07δ above the surface.

Downstream of the corner, the flow decelerates rapidly over the tail cone, with the boundary layer thickening, as seen in the streamwise mean velocity contours in Fig. 12. At the tail cone exit ($x/D = 3.17$) the boundary layer remains attached and is 79.5 mm thick; growing about 10 times the thickness just upstream of the corner, over a distance 1.2 D. Refer to Balantrapu et al. [13] for details on the evolution of the boundary layer over the strong adverse pressure gradient region.

However, the rotor noise is also expected to be a function of the size and convection speed of the anisotropic coherent structures ingested during operation. In general, this can be obtained experimentally by detailed measurements of the full 4-dimensional space-time correlation structure of the inflow turbulence, an enormous effort. However, representative subsets of such a measurement, can be extremely helpful in developing prediction methods. In our case, we measured a subset of the correlation structure of the streamwise unsteady velocity, just upstream of the rotor plane ($x/D = 3.17$), using the conventional two hotwire probe arrangement, explained in Section II.D. Additionally, we documented the large-scale convection velocities of the streamwise unsteady velocity. The streamwise length scales can be inferred from the integral time scales by invoking Taylor's hypothesis. The length scales, along the radius and circumference, are obtained by integrating the correlation coefficient over the probe separation. Such measurements have been performed at 4 anchor positions - 40, 65, 75, 85% of the boundary layer thickness at the rotor inflow plane ($x/D = 3.17$), results shown in Figures 14 and 15.

Fig. 14 shows the zero-time delay radial correlation statistics, with vertical axis representing the cross-correlation coefficient between the unsteady velocity seen by the probes ($\rho_{u_s u'_s}$) and the horizontal axis showing the radial separation ($r - r'$) normalized on the local boundary layer thickness (δ). Looking at the correlation coefficient

function, Fig. 14 b), at all anchor positions, the correlations decay monotonically, with no negative excursions except the outer 85% anchor position. Interestingly, the correlations decay to 10% over a radial separation of 0.2δ or 0.15 rotor radii R_{prop} , across all the anchor positions. The circumferential correlation coefficient is shown in a format similar to the radial correlations, in Fig. 15 b), with the horizontal axis representing the circumferential separation ($s = r\Delta\theta$) normalized on the boundary layer thickness. Generally, the circumferential correlation coefficient decays monotonically, producing negative tails unlike the radial case. Compared to the radial correlations, the circumferential correlations decay rapidly, reaching 10% levels at around 0.18 or 0.08 rotor radii, depending slightly on the anchor position. It appears that the radial length scales of the streamwise unsteady velocity are longer than the circumferential ones, more than twice, accounting for the negative lobes for the circumferential case.

B. Rotor Acoustics

All acoustic results presented are for $Re_D = 600k$ at a free stream velocity of 20.3 m/s. Thus, for these results, a change in advance ratio corresponds to a change in rotor rotational speed. To begin, Fig. 16 shows the noise measured by a single microphone with the rotor operating at $J = 1.44$ and $J = 1.13$ versus background spectra taken with the tunnel at speed with the rotor drive system on but not spinning. The broadband rotor noise could not be clearly distinguished from the background noise of the facility. Additionally, intense tones at the shaft rate, attributed to mechanical noise in the body of revolution tail cone, are present. At $J = 1.44$, portions of the spectra do increase above the background. As advance ratio decreases, noise levels increase at frequencies greater than the blade passage frequency (BPF) and there is perhaps some indication of haystacking, but in general, the noise source is unclear without beamforming. Therefore, to separate wind tunnel background, drive system background, and rotor noise sources, all data were processed with delay and sum beamforming using a grid in the vertical plane at $z = 0$ on the rotor axis. Frequency domain beamforming was used with the beamformer output b_j at grid point j given by

$$b_j = \vec{g}_j' \text{CSM} \vec{g}_j$$

where CSM is the cross spectral matrix of the microphone measurements, and \vec{g}_j is the grid steering vector given by

$$\vec{g}_j = \frac{1}{M} e^{-i\omega\vec{\tau}}$$

where ω is the angular frequency, M is the number of microphones in the array, and $\vec{\tau}$ is a vector of the expected time of flight between grid point j and each array microphone. In estimating τ , the speed of sound was corrected using the measured ambient temperature. The effect of convection and shear layer refraction on the sound path were accounted for using the method of Amiet [16]. Diagonal removal was also used on the cross spectral matrix. All beamforming was carried out in the AVEC Phased Array Software v4.10.

Background acoustic maps with the tunnel at speed and the rotor drive system on but not spinning are shown in Fig. 17. The maps were generated with the full array in $1/12^{\text{th}}$ octave-bands at center frequencies ranging from 335 Hz to 2000 Hz which correspond to $1 \times \text{BPF}$ for $J = 1.44$ to $5 \times \text{BPF}$ for $J = 1.13$. For these frequencies, the drive rig housing is identified as the dominant noise source; any noise sources on the body of revolution or in the vicinity of the rotor are at least 10 dB down in the map from those identified on the drive rig. Above 1000 Hz, sources are localized to the swept leading and trailing edges of the drive rig as well as the housing/rotor shaft junction suggesting flow generated noise.

Operating the rotor at $J = 1.44$, Fig. 18 shows beamforming maps at the BPF and harmonics for different components of the 251-channel array: four separate spirals numbered 1 through 4 and the full array (all maps are on a 10 dB dynamic scale with the map maximum indicated above each map). Spiral 4 maps are indicative of a source further downstream than the extents of the spiral but are smeared because of the array point spread function. Further the receiving path from the rotor to Spiral 4 is obscured by the body of revolution. Spirals 1, 2, and 3 have more favorable point spread functions and distinguish the rotor source at $2 \times \text{BPF}$ and above. The full array works well at all frequencies above the BPF and though not representative of a single receiver location provides the best streamwise resolution. Multiple lobes appear in the maps for the full array because sources received by the full array are likely distributed across the entire blade disk. Therefore, results will be presented for the full array and Spiral 2 as representative of observed changes to noise production. Spiral 2 is more indicative of sound received at a more compact receiver area.

Acoustic maps for Spiral 2 and the full array for conditions of decreasing advance ratio are shown in **Fig. 19** and **Fig. 20**, respectively. The maps from both arrays indicate noise from the rotor area at lower advance ratios, but results are more definitive at higher frequency (lower beamwidth). Drive and mount system noise is significant at low frequencies < 670 Hz and between 800 and 1400 Hz, but rotor noise at the higher frequency range is separable from the drive rig. Both arrays indicate a noise source at the nose of the body of revolution at 1250 Hz that is not identified in the background (Fig. 18). The tighter streamwise beamwidth of the of full array resolves an additional source at

1250 Hz half way up the nose and also appears to identify the same set of sources at 800 Hz. These center frequencies about harmonics of the BPF include the shaft rate tones observed in the single mic spectra. However, narrowband (6.25 Hz resolution) beamform maps clearly identify a significant noise in the rotor area at frequencies from 600 to 2100 Hz even when not at the shaft rate tones, indicating that substantial broadband rotor noise was measured. Figure Fig. 21 shows narrowband acoustic maps for $J = 1.27$. When near the 2 x BPF frequency, but not exactly at a shaft rate harmonic (Fig. 21 a), a region encompassing the rotor is identified as the source. In contrast, when near 2 x BPF and directly on a shaft rate harmonic (Fig. 21 b), the identified source region shifts off the rotor onto the aft of the body of revolution. This shifting of the identified source from the rotor to the body of revolution aft when at shaft rate harmonics occurs consistently from 600-2100 Hz for $J = 1.44, 1.27$ and 1.13 , suggesting that the shaft rate tones are a product of mechanical noise originating in the body.

Given these results, an integration window was defined to contain the rotor noise source identified with Spiral 2 in the 2 x BPF, $J = 1.44$ map (lowest frequency BPF with source identified) and used to compute integrated spectra for all advance ratios. As shown in and Fig. 20, the integration region extends 0.66 m forward and 0.33 m aft of the rotor in the streamwise direction and ± 0.5 m vertically off the rotor axis. The beamwidth at this frequency is also indicated for reference. Within this integration region, the observed source region may be influenced by the body of revolution but separation with drive rig system is still apparent. The integration procedure was carried out in the AVEC Phased Array Software v4.10 and is based on the theory described by Dougherty [17]. An integration cutoff of 10 dB was used.

Integrated spectra for decreasing advance ratio are presented in Fig. 22. Compared to the single microphone spectra, tones at the shaft rate are still present but there is now a clear broadband noise increase at frequencies above the BPF that increases with decreasing advance ratio. Removing all tones within 1 bin (6.25 Hz) of the shaft rate, no wider than 4 bins (25 Hz), and at least 1.5 dB above surrounding points, reveals haystack-like structures organized around the first 3 BPFs but with peaks significantly shifted above the BPF. These haystack structures increase in amplitude with decreasing advance ratio but remain broad. The frequencies of the haystack peaks are shifted up by ~ 7 -12% of the BPF. For comparison, the integrated spectra with tone removal procedure applied for decreasing advanced ratio are plotted together in Fig. 23 a) normalized on the BPF. In addition, spectra generated using the same integration region but full array are shown in Fig. 23 b). Similar haystacking results are found with the full array but relative amplitude changes could be influenced by shifts in the amplitudes across the array, shifting sources and changes with J . The full array spectra are smoother with the haystack peaks more easily identified.

Haystacking in the spectra suggests that the turbulent structures in the inflow are of sufficient scale to be cut multiple times as they convect through the rotor resulting in correlated blade-to-blade loading. Haystacks increase in level as the rotor angular velocity increases (decreasing J), turbulent structures are sliced more times as they pass through the rotor. Blue-shifting of the broadband spectra is expected due to rotor response bias of the inflow turbulence. Murray et al. [19] detail the relationship of the sectional rotor response to the angle of incidence of an inflow gust. They show that the blade-relative unsteady upwash velocity is greater for eddies which interact with the blades at a rate greater than the BPF. This produces a stronger blade response, and therefore, the haystacks in the broadband spectra shift to frequencies slightly greater than the BPF.

IV. Conclusions and Ongoing Work

Aerodynamic and acoustic measurements have been completed for a body of revolution which is being used to generate a thick axially symmetric boundary layer. This inflow is used to study the turbulence ingestion noise produced by a rotor at zero thrust and thrusting advance ratios. The rotor operation is expected to be coupled to the evolution and development of the baseline inflow turbulence. Measured data include of the body, single and quadwire boundary layer profiles along the tail cone region, unsteady surface pressure on the tail cone, far field phased array acoustic measurements, and PIV in the tail cone region. Baseline inflow data were acquired without the rotor. These data show the development of a thick boundary layer which is as large as the rotor span, such that the rotor blades are entirely immersed in turbulent flow at the zero-thrust condition. These data also show that the boundary layer maintains a small normal-to-wall velocity gradient without separating. The undisturbed turbulence stress profiles have a broad slowly varying shape across much of the blade span at the location of the rotor disk with peak turbulence intensities near 10% of the freestream velocity. The measured convection velocity profile indicate that coherent turbulent structures convect at the mean local velocity except for locations very near the wall which have a slightly higher normalized convection speed. Acoustic data show broadband turbulence ingestion noise and haystacks corresponding to the correlated blade interaction with large scale structures. The peaks of the observed haystacks are harmonics of each other but are shifted in frequency 7-12% of the blade passage frequencies. Analysis of the aerodynamic and acoustic measurements is ongoing. Measured inflow turbulence characteristics will be used to predict the far field noise through methods such as Glegg et al. [18] for comparison with measured acoustic data

Acknowledgments

The authors would like to thank the Office of Naval Research for sponsoring this work under grants N00014-17-1-2698 and N00014-17-1-2682 particularly Drs. Ki-Han Kim and John Muench. Authors are grateful to Vidya Vishwanathan, Aldo Garguilo, Nandita Hari, Matthew Ruda, James MacDonald amongst others for their assistance during the wind tunnel experiments. The authors would also like to thank Mr. Michael Marcolini, and Drs. William Blake, Meng Wang and Jason Anderson for their helpful advice and guidance on this project.

References

- [1] Pagano, A., Barbarino, M., Casalino, D., and Federico, L., "Tonal and broadband noise calculations for aeroacoustic optimization of a pusher propeller," *Journal of Aircraft*, 2010, vol. 47, no. 3, pp. 835-848.
- [2] Sevik, M., "Sound Radiation from Subsonic Rotor Subjected to Turbulence," in *International Symposium on Fluid Mechanics and Design of Turbomachinery*, University Park, Pennsylvania, 1973.
- [3] Hanson, D.B., "Spectrum of Rotor Noise Caused by Atmospheric Turbulence," *Journal of the Acoustical Society of America*, 1974, vol. 56, no. 1, pp. 110-136.
- [4] Majumdar, S.J., and Peake, N., "Noise Generation by the Interaction between Ingested Turbulence and a Rotating Fan," *Journal of Fluid Mechanics*, 1998, vol. 359, pp. 181-216.
- [5] Blake, W., *Mechanics of Flow Induced Sound and Vibration*, Orlando, FL: Academic Press, 1986.
- [6] Martinez, R., "Broadband Sources of Structure-Borne Noise for Propulsors in "Haystacked" Turbulence," *Computers and Structures*, 1997, vol. 65, no. 3, pp. 475-490.
- [7] Glegg, S., and Walker, N., "Fan Noise from Blades Moving Through Boundary Layer Turbulence," in 5th AIAA/CEAS Aeroacoustics Conference, Bellevue, Washington, 1999.
- [8] Joseph, P., and Parry, A., "Rotor/Wall Boundary-Layer Interaction Broadband Noise in Turbofan Engines," in 7th AIAA/CEAS Aeroacoustics Conference, Maastricht, Netherlands, 2001.
- [9] Atassi, H.M., and Logue, M.M., "Fan Broadband Noise in Anisotropic Turbulence," in 15th AIAA/CEAS Aeroacoustics Conference, Miami, Florida, 2009.
- [10] Devenport, W.J., Burdisso, R.A., Borgoltz, A., Ravetta, P.A., Barone, M.F., Brown, K.A., and Morton, M.A., "The Kevlar-walled anechoic wind tunnel," *Journal of Sound and Vibration*, 2013, vol. 332, no. 17, pp. 3971-3991.
- [11] Hammache, M., Browand F.K., Blackwelder R.R., "Whole-field velocity measurements around an axisymmetric body with a Stratford-Smith pressure recovery." *Journal of Fluid Mechanics*, 2002, vol 461, pp.1-24.
- [12] Wittmer, K. S., Devenport W.J., Zsoldos J.S., "A four-sensor hot-wire probe system for three-component velocity measurement." *Experiments in Fluids*, 1998, vol 24, no. 5, pp. 416-423,
- [13] Balantrapu, N. A., Hickling C.J., Millican A.J., Alexander W.N., Lowe K.T., Devenport, W.J., and Glegg, S.A.L., "Turbulent Boundary Layer in a Strong Adverse Pressure Gradient over a Body of Revolution." 11th International Symposium on Turbulence and Shear Flow Phenomena, 2019 (under review)
- [14] Bearman, P. W. "Corrections for the effect of ambient temperature drift on hot-wire measurements in incompressible flow." *DISA Information*. 1971, vol.11, pp 25-30.
- [15] Wang, M., Personal Communication, Nov. 2018.
- [16] Amiet, R.K., "Refraction of Sound by a Shear Layer", *Journal of Sound and Vibration*, 1978, vol. 58, pp. 467-482.
- [17] Thomas Mueller (ed.), *Aeroacoustic Measurements*, Springer, 2002. ISBN 3-540-41757-5.
- [18] Glegg, S.A.L., Devenport, W.J., and Alexander, W.N., "Broadband Rotor Noise Predictions Using a Time Domain Approach", *Journal of Sound and Vibration*, 2015, vol. 335, pp. 115-124.
- [19] Murray, H., Devenport, W.J., Alexander, W.N., Glegg, S.A.L., and Wisda, D., "Aeroacoustics of a Rotor Ingesting a Planar Boundary Layer at High Thrust", *J. Fluid Mech.*, 2018, vol. 850, pp. 212-245.

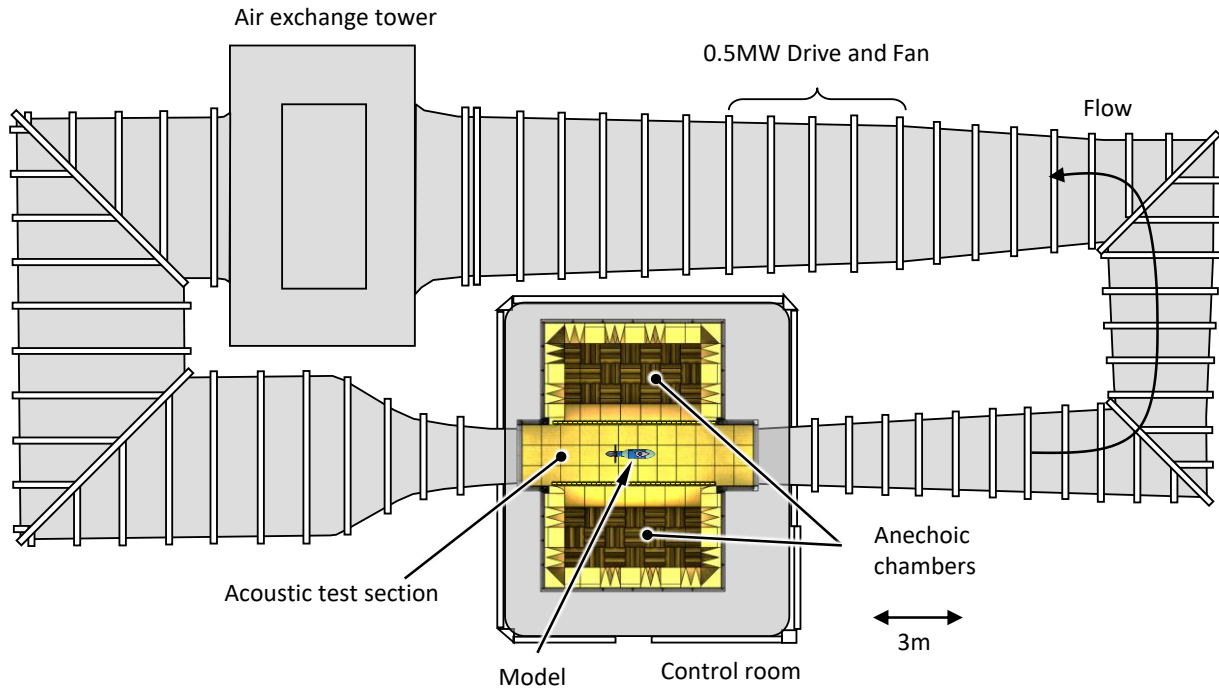


Fig. 1: Plan view of Virginia Tech Stability Wind Tunnel in full anechoic configuration

Phased microphone array

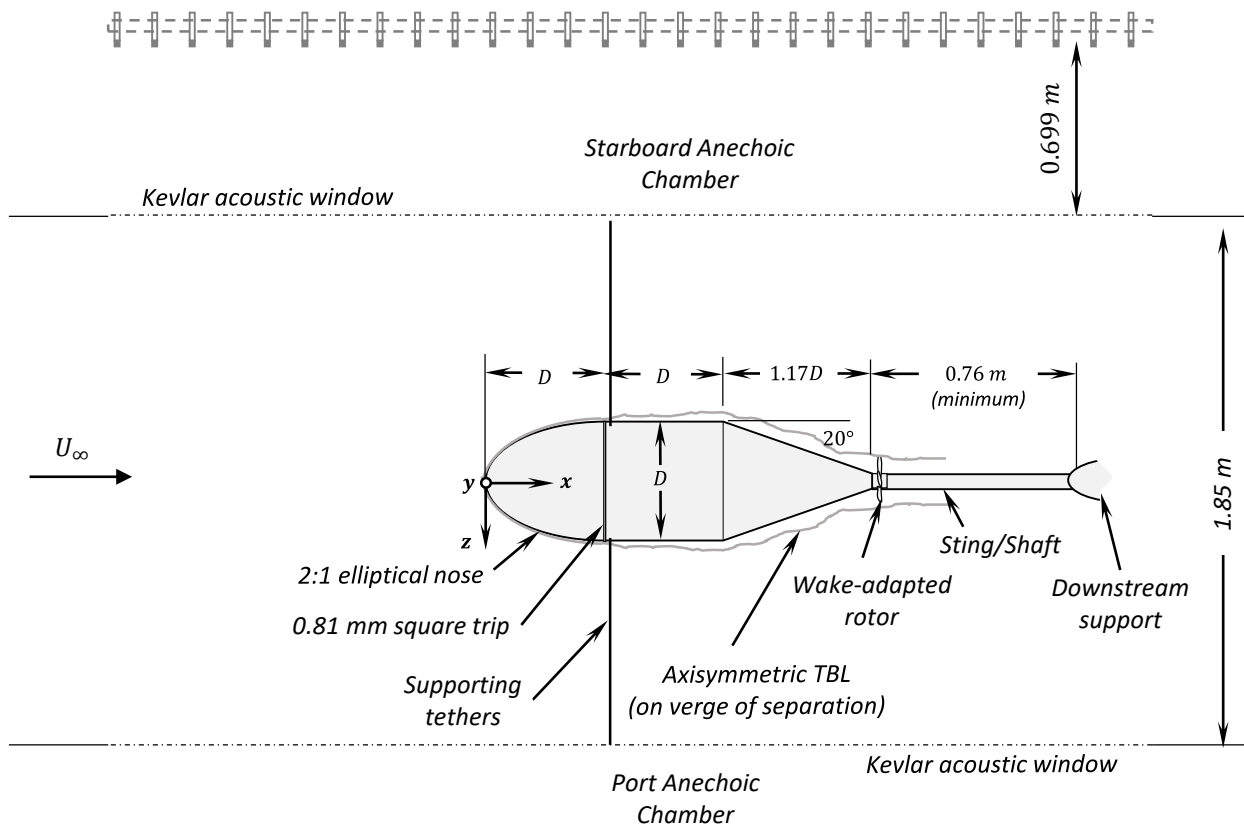


Fig. 2: Plan view of body of revolution as installed in Virginia Tech Stability Wind Tunnel. The coordinate system used in presenting all experimental results is shown at the nose of the body

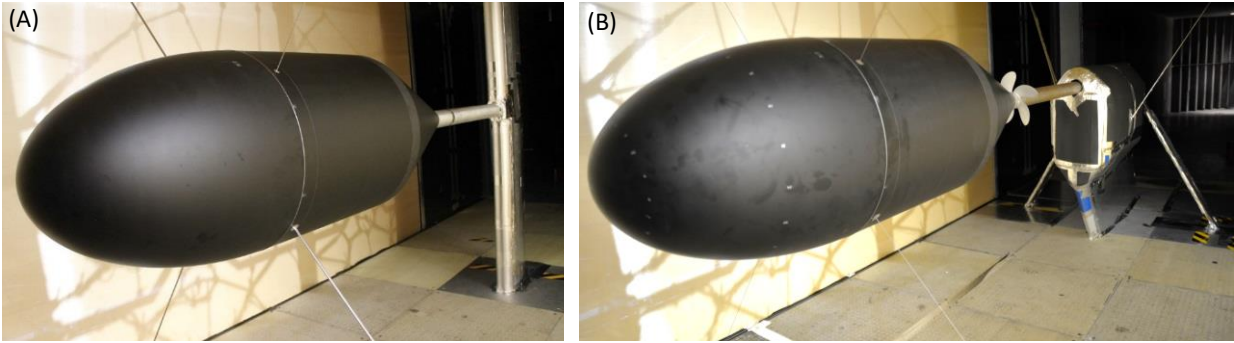


Fig. 3: Body of revolution mounted in the Virginia Tech Stability Wind Tunnel and supported downstream by A) a static sting and support for measurements without the rotor present and B) a drive rig with hollow shaft for measurements with the rotor spinning



Fig. 4: CAD of rotor wake-adapted to operate in the boundary layer of the body of revolution

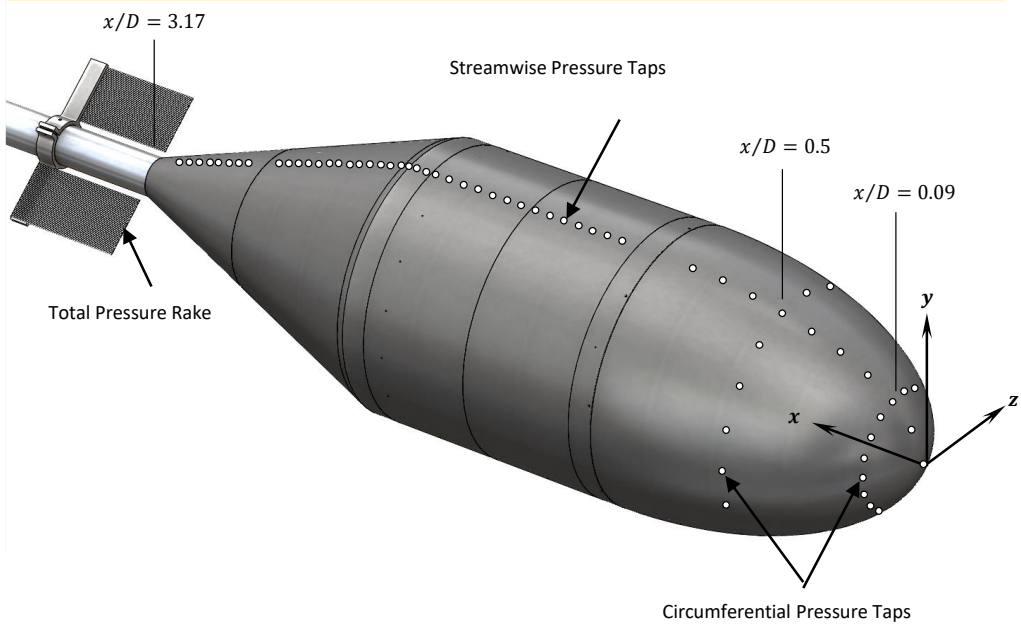


Fig. 5: Body of revolution surface pressure instrumentation: 51 streamwise pressure taps, two circumferential rings of 16 pressure taps each on the nose and a 119 port total pressure rake in the wake of the body.

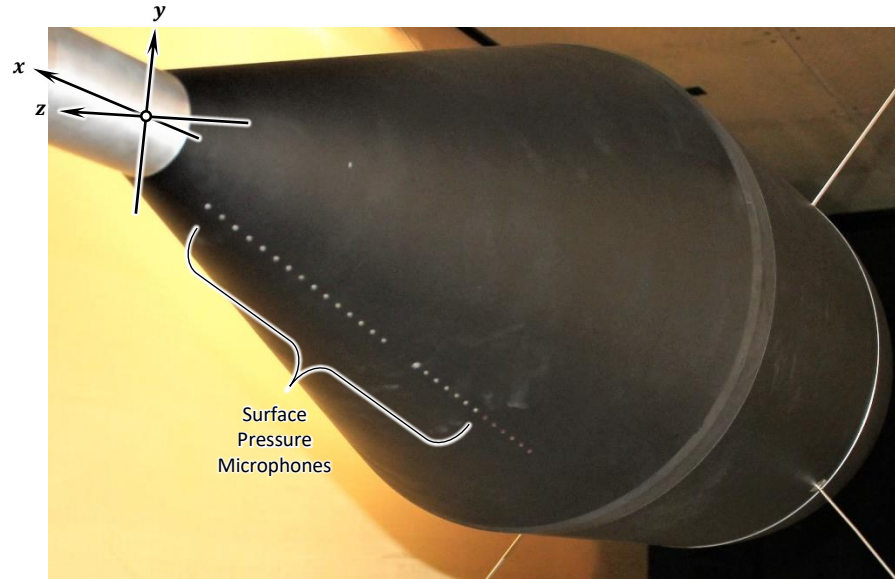


Fig. 6: Experimental photograph of streamwise array of flush-mounted Sennheiser microphones used to measure the unsteady surface pressure over the body of revolution tail cone

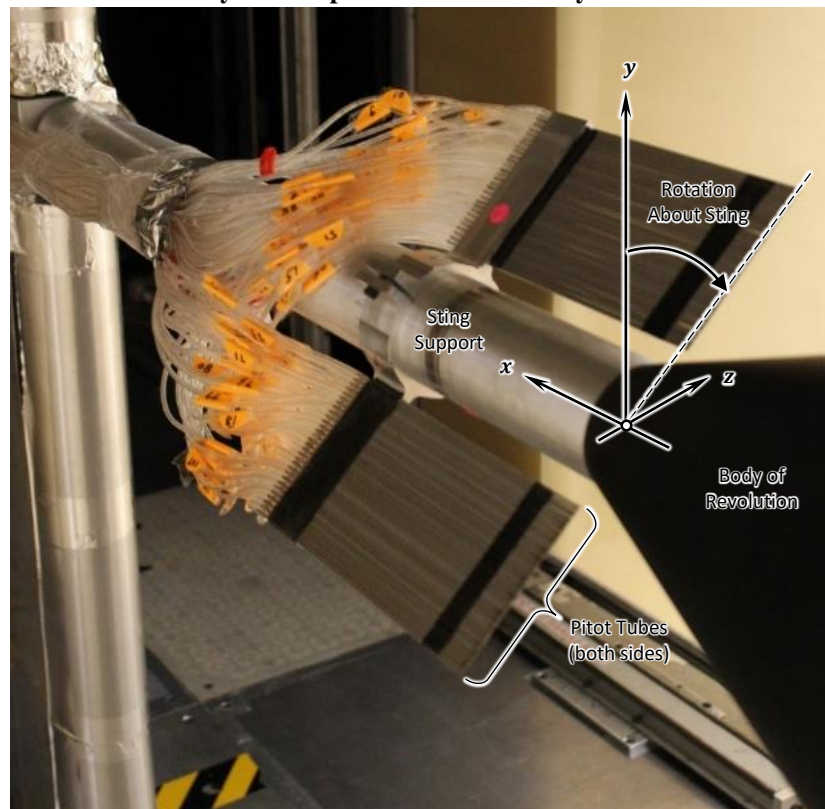


Fig. 7: Experimental photograph of custom-built total pressure rake used to measure the wake of the body of revolution

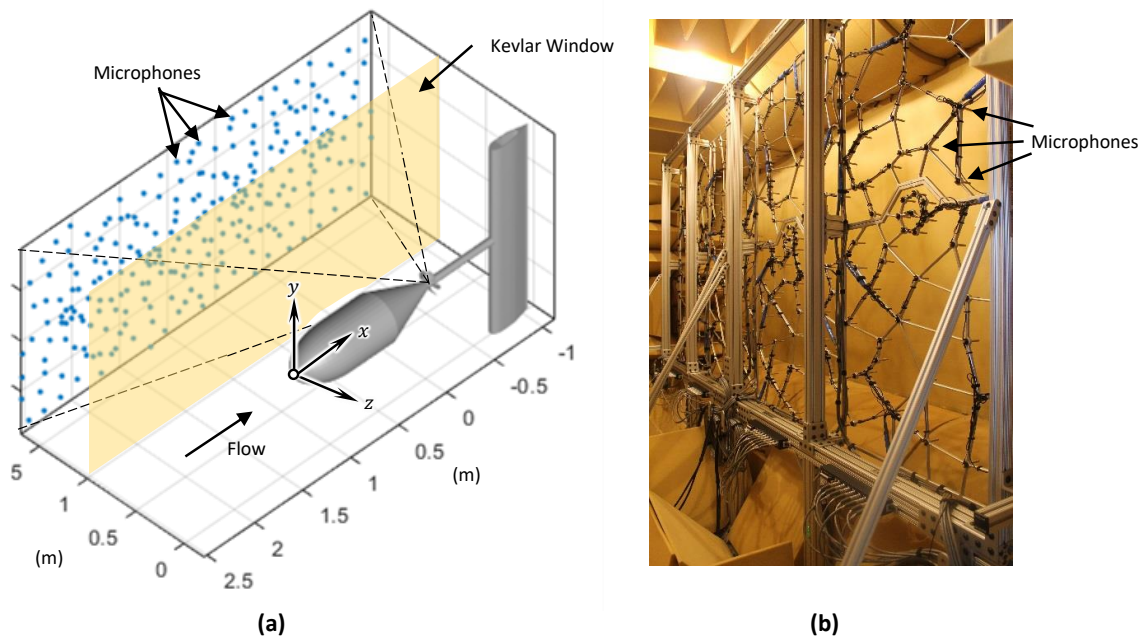


Fig. 8: (a) Microphone array setup diagram and (b) microphone array in starboard anechoic chamber

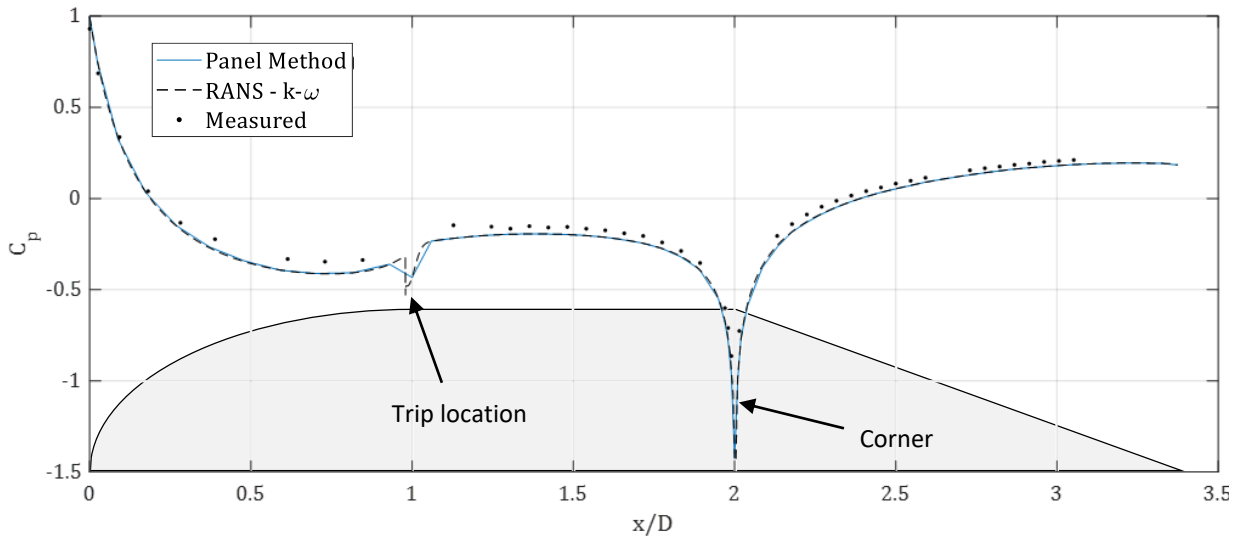


Fig. 9: Mean pressure distribution over the body measured the streamwise array or pressure ports. Results are compared with Ideal flow panel method calculations and RANS estimates (private communication)

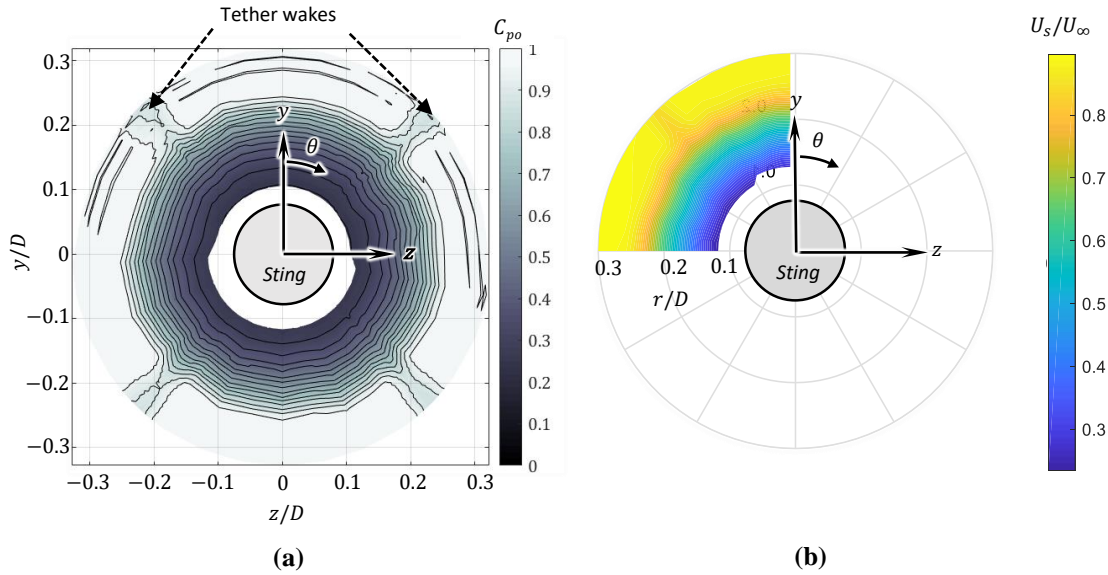


Fig. 10: Measurements of axial symmetry at the tail cone exit ($x/D = 3.17$): a) Contours of stagnation pressure coefficient, including wakes from old tethers. b) Contours of streamwise mean velocity over a quadrant, including the wake from a new tether. Coordinate system in global convention

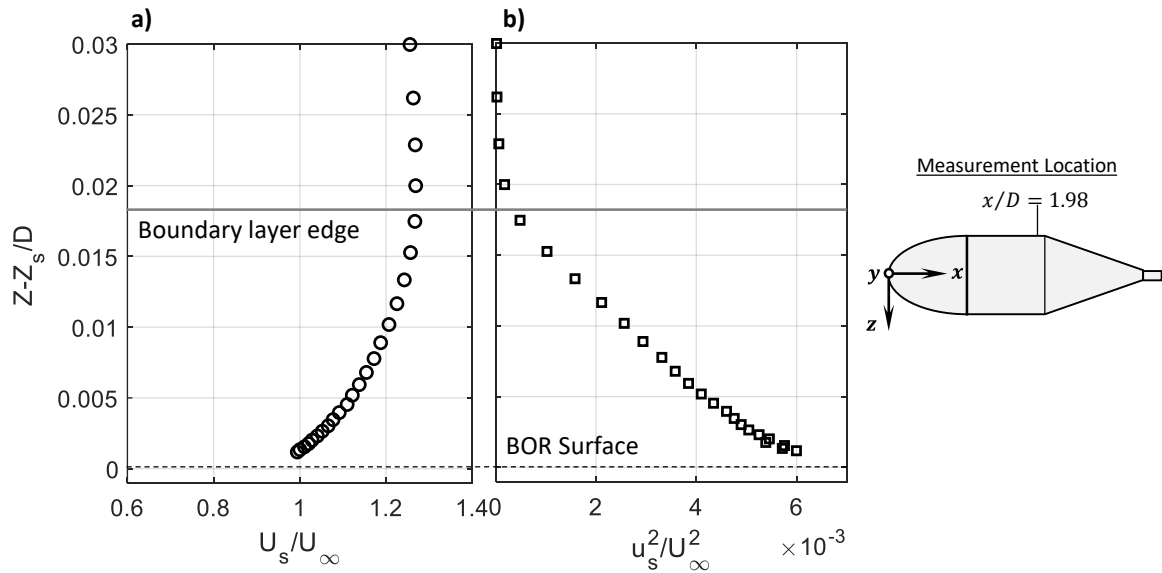


Fig. 11: Boundary layer statistics just upstream of the corner. a) Streamwise Mean Velocity, normalized on the tunnel inlet velocity; b) Streamwise Reynolds normal stresses normalized on the tunnel inlet velocity

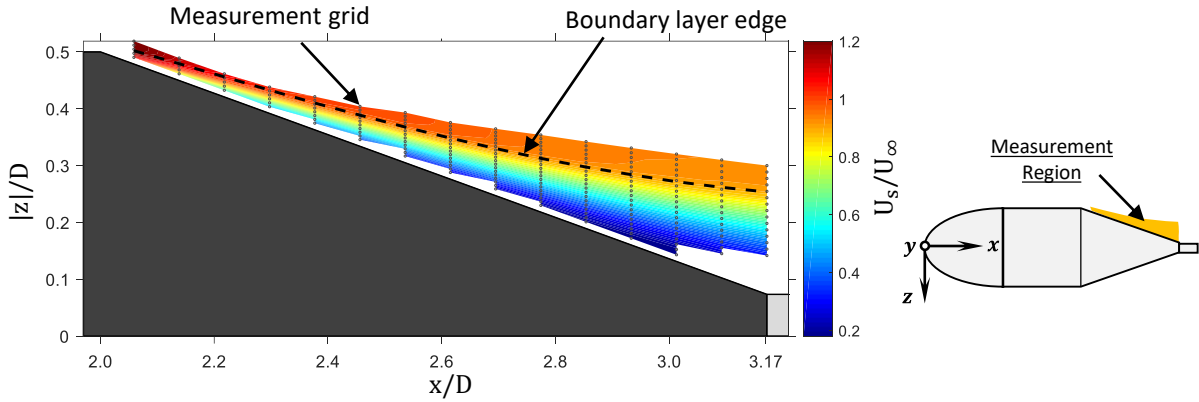


Fig. 12: Contours of the streamwise mean velocity over the tail cone. Measurement region highlighted in the thumbnail

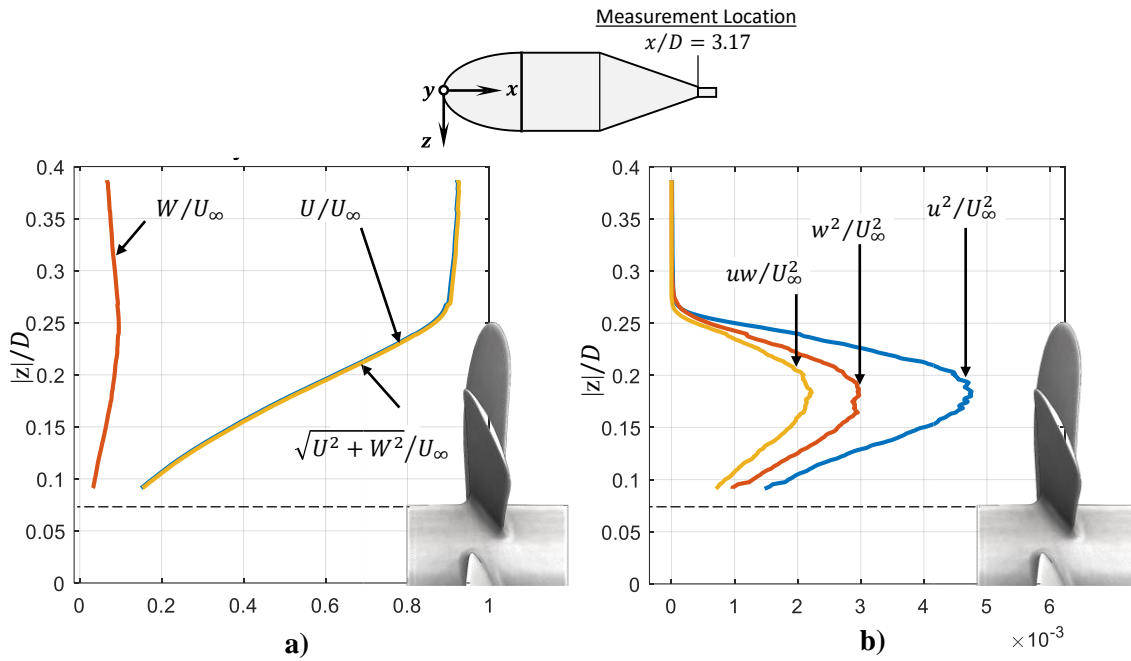


Fig. 13: a) Mean velocity profile (U, W) at the tail cone exit, just upstream of the intended rotor location. b) Reynolds normal stresses and in-plane shear stresses, normalized on the tunnel inlet velocity; Shown with reference to the blade radius

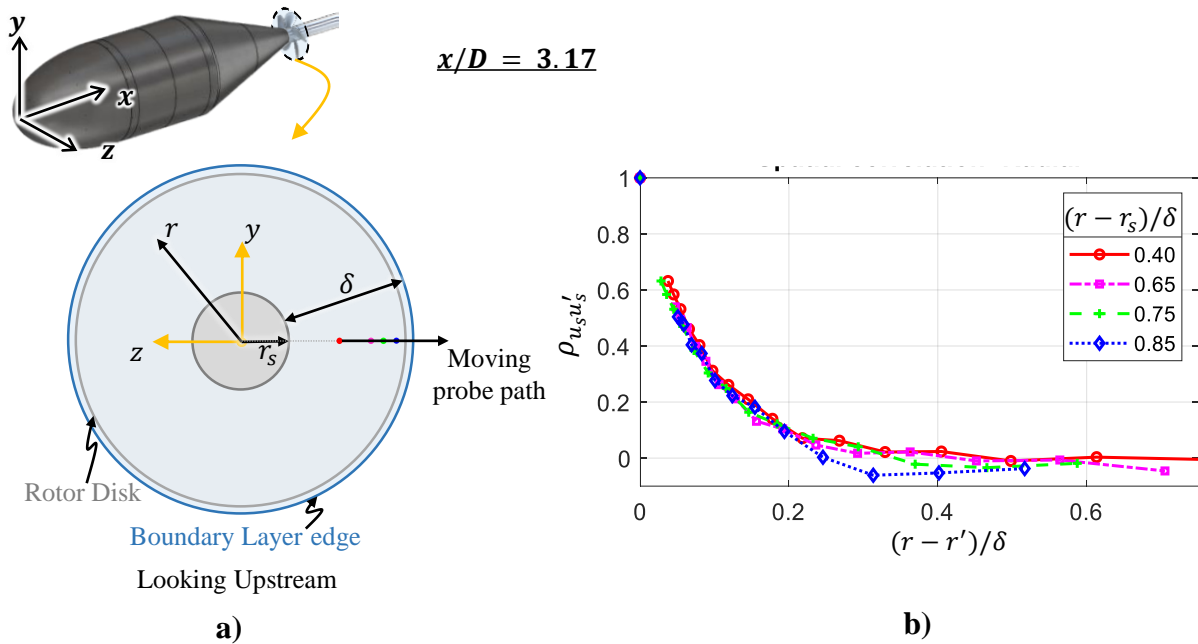


Fig. 14: Zero-time delay, radial correlation measurements at the tail cone exit. a) Thumbnail showing the measurement plane, fixed probe positions and moving probe path. b) Radial correlation coefficient profiles at each anchor point (40, 65, 75, 85% δ) as a function of radial separation ($r - r'$) between the two probes, normalized by the local boundary layer thickness (δ).

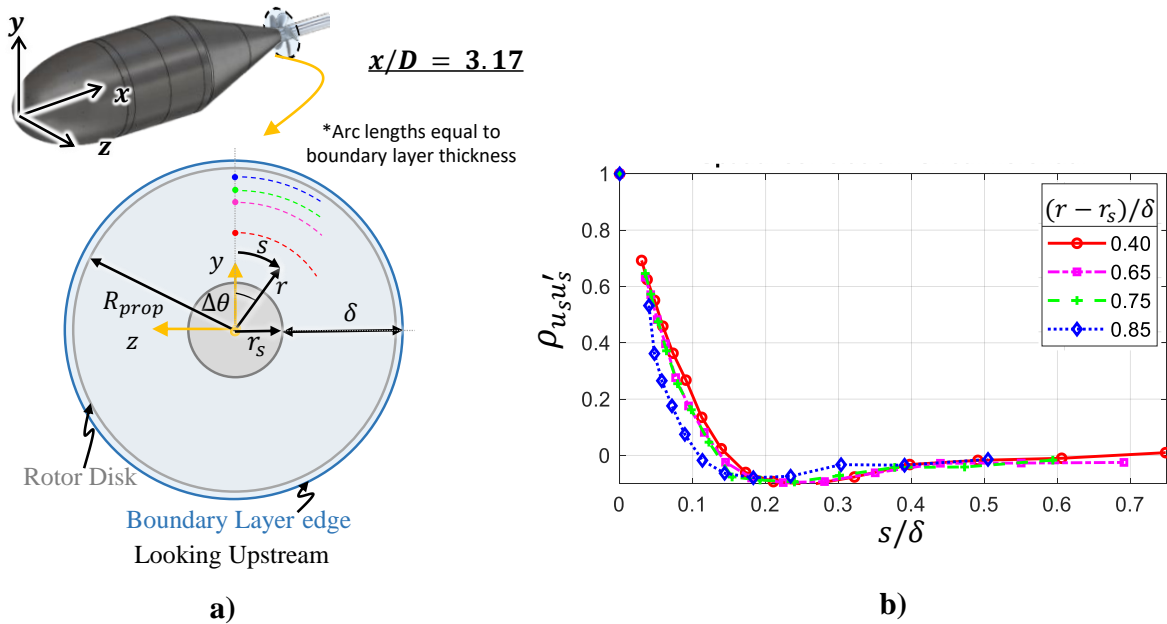


Fig. 15: Zero-time delay, circumferential correlation measurements at the tail cone exit. a) Thumbnail showing the measurement plane, fixed probe positions and moving probe path. b) Circumferential correlation coefficient profiles at each anchor point (40, 65, 75, 85% δ) as a function of circumferential separation ($s = r\Delta\theta$) between the two probes, normalized by the local boundary layer thickness (δ).

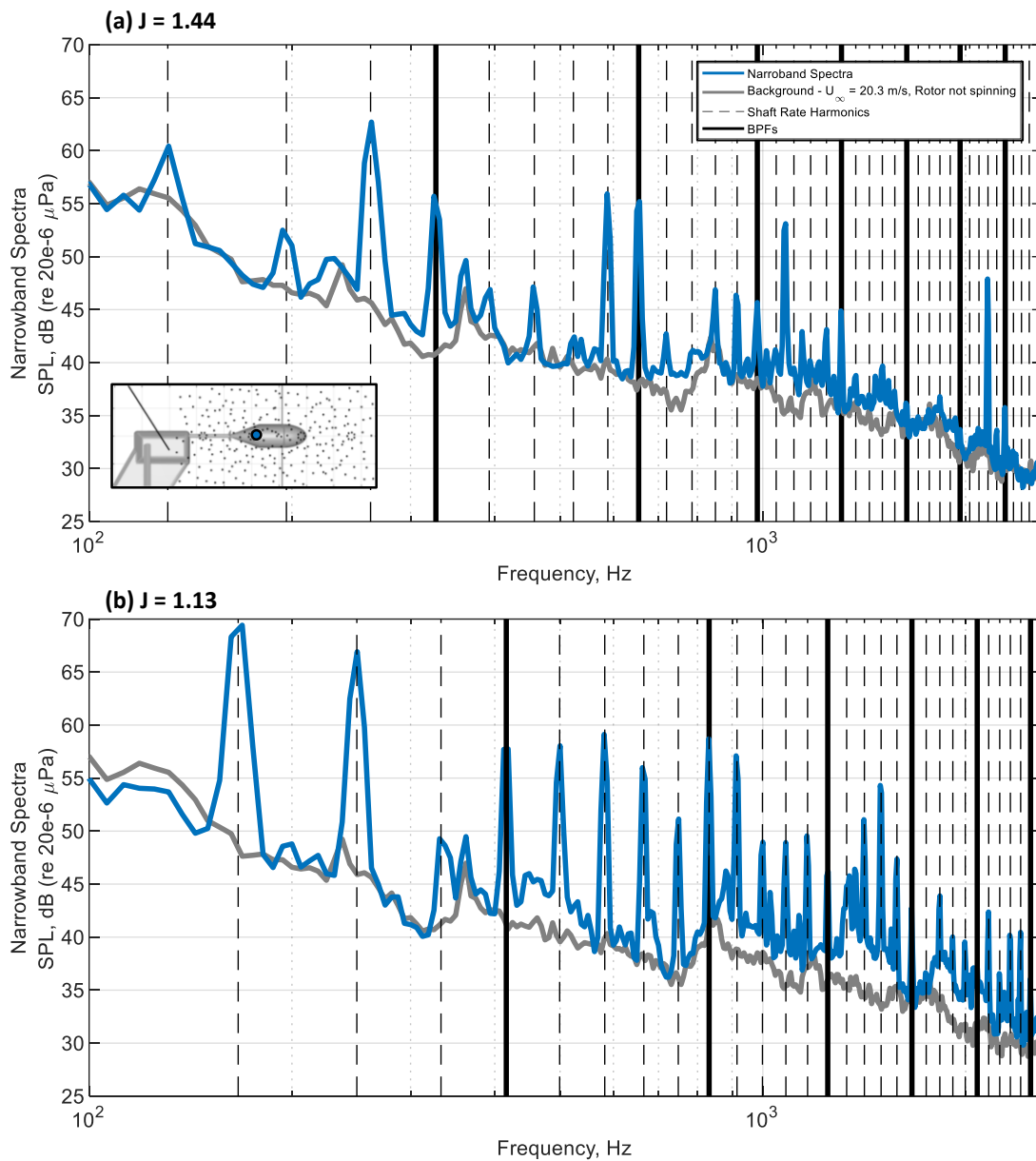


Fig. 16: Noise measured by a single microphone upstream of the rotor plane (see inset) for a) zero thrust condition, $J = 1.44$, 3926 rotor RPM and b) moderate thrust condition $J = 1.13$, 3992 rotor rpm. Both conditions are for a freestream velocity of 20.3 m/s and are plotted against a background noise measurement at same free stream velocity but with the rotor not spinning.

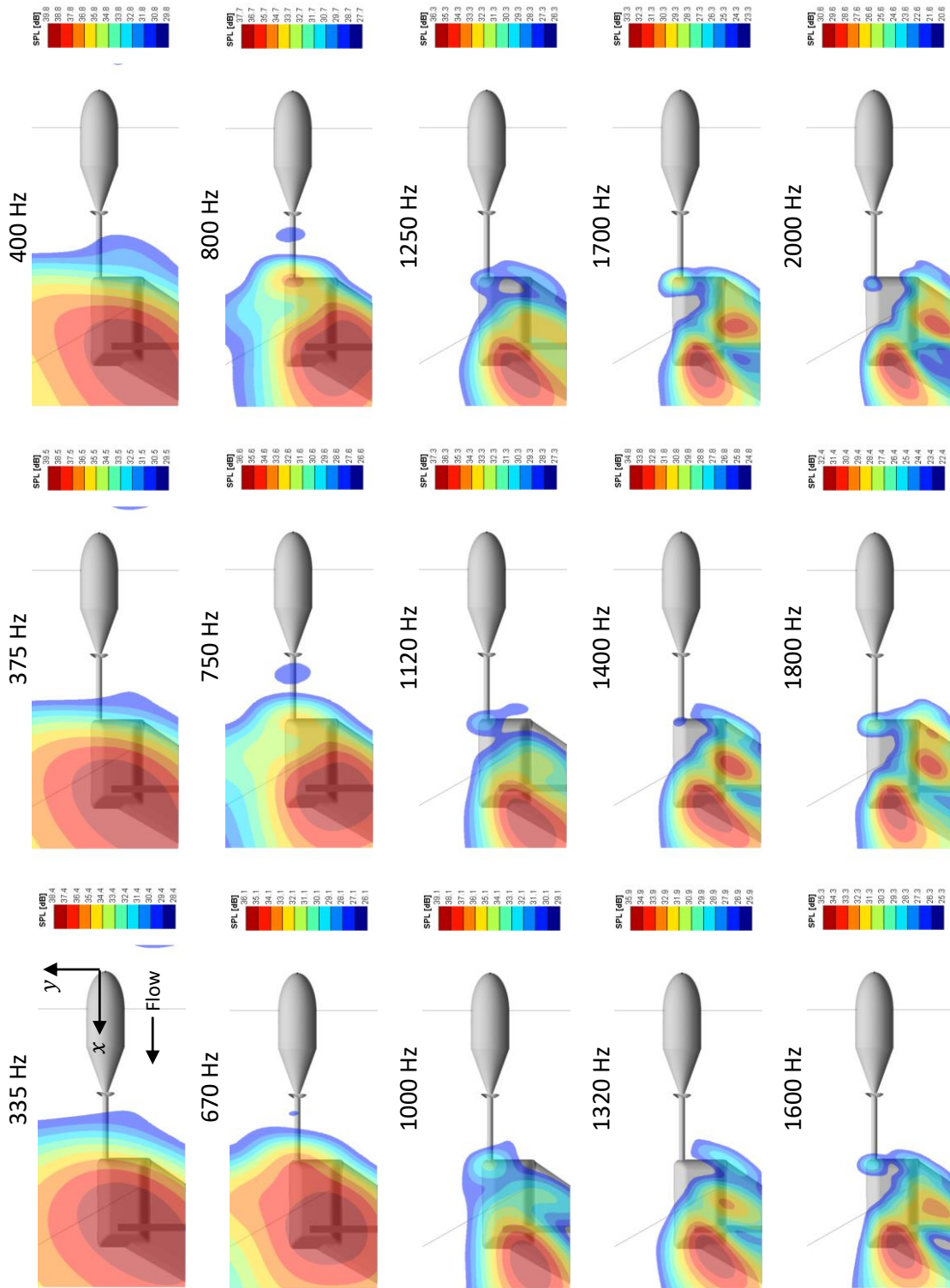


Fig. 17: 1/12th octave beamforming generated using the full 251-channel array at a background condition with the tunnel at 20.3 m/s and the rotor drive system on but not spinning.

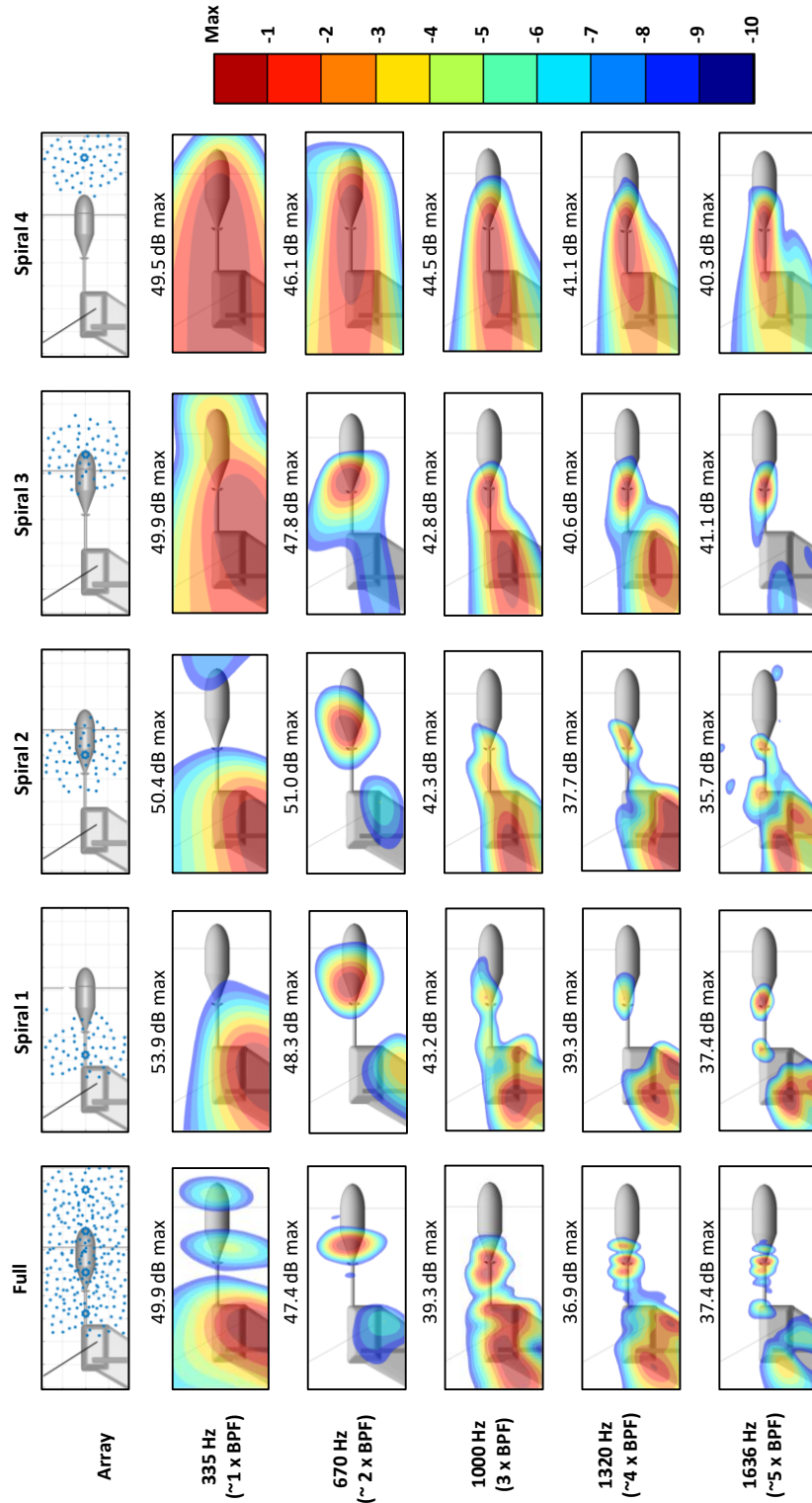


Fig. 18: 1/12th octave beamforming maps generated using different components of the 251-channel array at the BPF's and harmonics with $J = 1.44$

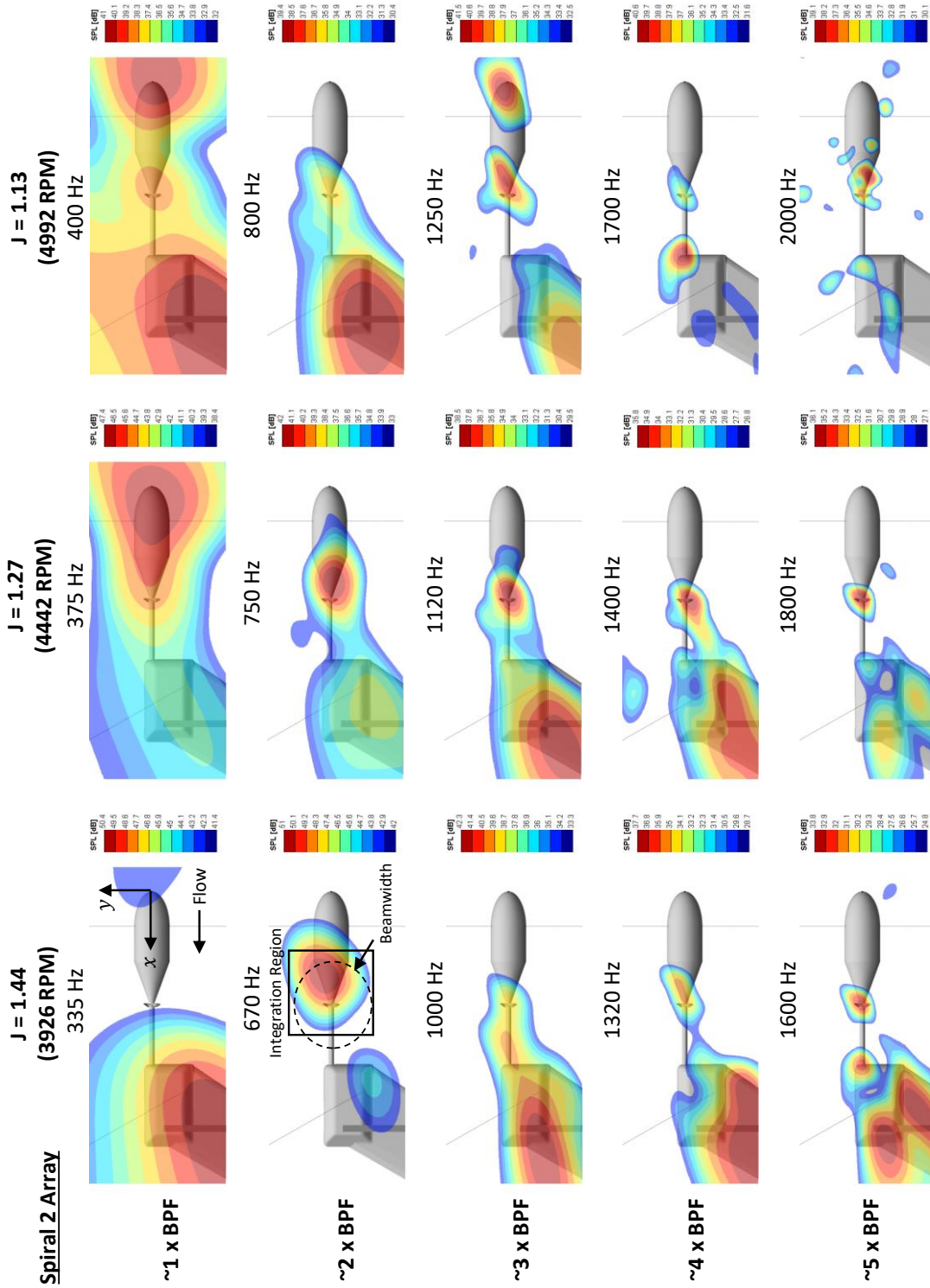


Fig. 19: 1/12th octave beamforming maps for decreasing advance ratio at BPF and harmonics generated using the Spiral 2 subarray

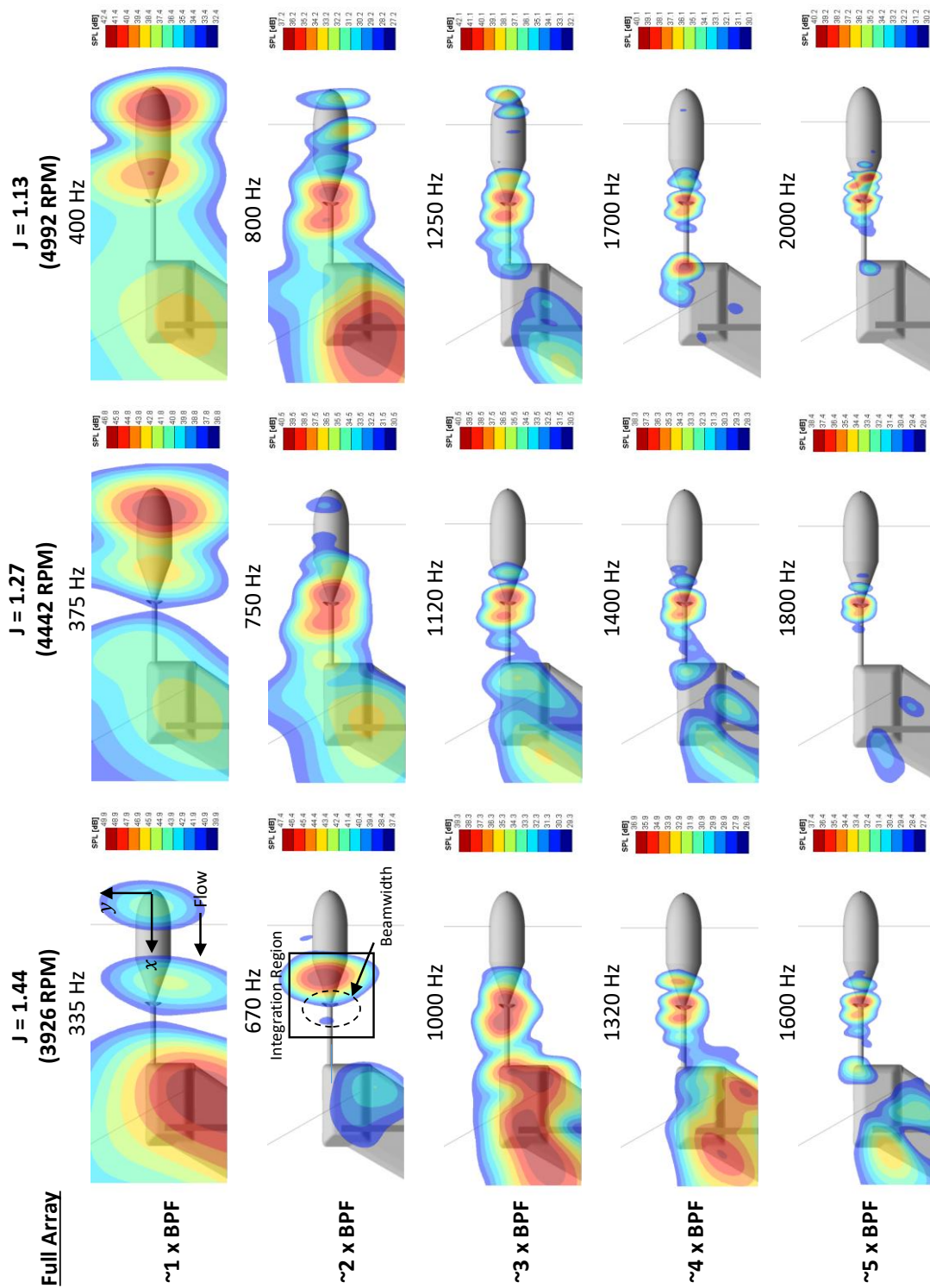


Fig. 20: $1/12^{\text{th}}$ octave beamforming maps for decreasing advance ratio at BPF and harmonics generated using the full array

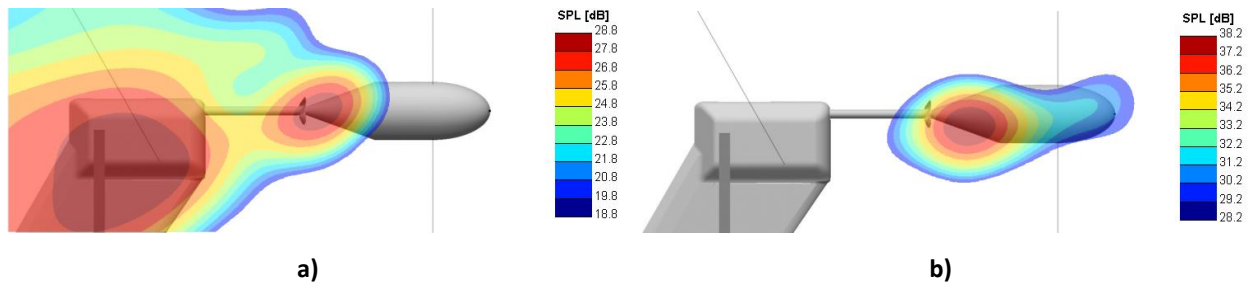


Fig. 21: Narrowband beamforming maps for $J = 1.27$ generated using the Spiral 2 subarray at a) 725 Hz near $2 \times \text{BPF}$ (731 Hz) but not exactly at shaft rate harmonic and b) 737.5 Hz near $2 \times \text{BPF}$ but exactly at a shaft rate harmonic

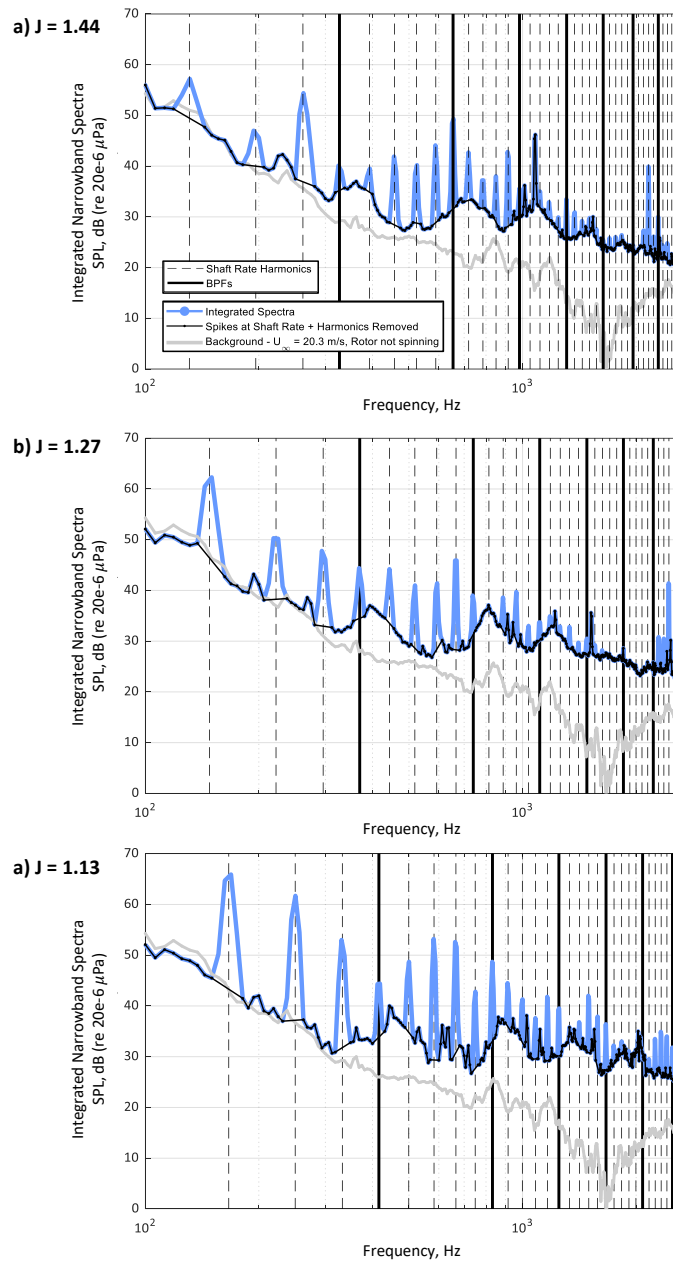


Fig. 22: Integrated spectra for decreasing advanced ratio generated using Spiral 2 beamforming maps

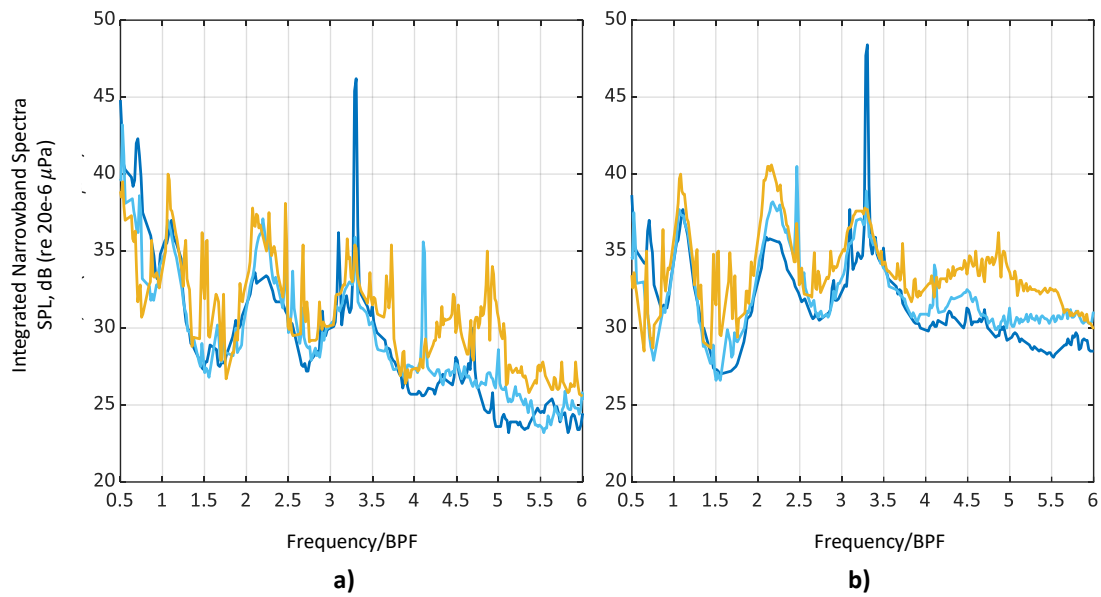


Fig. 23: Integrated spectra a) from Spiral 2 and b) from full array for decreasing advanced ratio normalized on the BPF. Tones at the shaft rate have been removed.